PHYSICAL REVIEW B **79**, 104520 (2009)

Vortex matter in a hybrid superconducting/ferromagnetic nanostructure

Q. H. Chen,[1] C. Carballeira,[2,*] and V. V. Moshchalkov[1]
[1]*INPAC-Institute for Nanoscale Physics and Chemistry, Nanoscale Superconductivity and Magnetism Group, K. U. Leuven, Celestijnenlaan 200 D, 3001 Leuven, Belgium*
[2]*Departamento de Física da Materia Condensada, LBTS, Universidade de Santiago de Compostela, Santiago de Compostela E-15782, Spain*

(Received 2 December 2008; revised manuscript received 25 February 2009; published 26 March 2009)

By using a gauge transformation of the vector potential that accounts for the superconducting/vacuum boundary condition, we solve the linear and nonlinear Ginzburg-Landau equations to calculate the phase diagram of the hybrid superconducting/ferromagnetic nanostructure formed by a superconducting microsquare with a magnetic disk on top. Close to the normal/superconducting phase boundary $[T_c(H)]$ we observe that the competition between the applied magnetic field and the inhomogeneous field of the disk strongly affects the vortex nucleation. As a consequence, different symmetry constraints are imposed on the vortex patterns at $T_c(H)$, leading to the exclusion of some vorticity values allowed in the no-dot case. The dot also influences the evolution with temperature of the vortex states deep in the superconducting phase, giving rise to instability processes that differ from those previously found in individual microsuperconductors and that may involve the spontaneous generation of additional vortices. Besides, the dot also forces the vortex matter in this hybrid nanostructure to behave similarly to the case of an individual microdisk in some regions of the phase diagram.

DOI: 10.1103/PhysRevB.79.104520 PACS number(s): 74.20.De, 74.25.Dw, 74.78.Na, 75.75.+a

I. INTRODUCTION

The behavior of a superconductor in the vicinity of a ferromagnet is one of the aspects of the physics of superconductivity that has been intensively studied during the recent years.[1] When both materials are in contact, the superconducting and magnetic order parameters will be coupled via the exchange in electrons (the so-called proximity effect[1]) giving rise to different physical phenomena as, for instance, spin-switch superconductivity.[2] This direct coupling can be suppressed by separating the superconductor from the ferromagnet, and then, the interaction between both materials is reduced to the electromagnetic effect of the inhomogeneous field of the dot on the superconducting condensate.[1] However, even in that case the influence of the ferromagnet may significantly affect the behavior of a superconducting material. In particular, the compensation of the stray field of the ferromagnet with an external homogeneous field may induce the appearance of local domains in the superconductor where the total magnetic field is negligible and, thus, where the nucleation of superconductivity is favored.[3] This can lead, among other effects, to nonconventional normal/superconducting phase boundaries $[T_c(H)]$ (Refs. 4 and 5), magnetic-field-induced superconductivity,[6] or field polarity-dependent superconductivity.[7]

The interest for the interaction between superconductivity and magnetism has been also extended to hybrid superconducting/ferromagnetic (S/F) nanosystems. Previous works on individual microsuperconductors have shown that the superconducting critical parameters (critical temperature T_c, field H_{c2}, and current J_c) can be considerably modified through nanostructuring.[8,9] For instance, when the size of a thin superconductor becomes of the order of the coherence length, $\xi(T)$, its normal/superconducting phase boundary shows a cusplike behavior superimposed onto a linear background, each of the cusps corresponding to a change in the fluxoid quantum number (also called vorticity, L) by one.[8,9] Different studies performed within the framework of the phenomenological Ginzburg-Landau (GL) theory have also demonstrated that the confinement of the superconducting condensate may induce some peculiar changes in the vortex matter of these systems. In particular, it has been found that close to $T_c(H)$, where the GL theory may be applied in its linearized form, giant vortex and vortex-antivortex pairs can be spontaneously generated in superconducting microdisks[10–12] and, respectively, mesoscopic regular polygons (as triangles[13–15] and squares[15–18]) to comply with the symmetry of the sample. Deeper in the superconducting phase the nonlinear effects associated with high order terms in the GL free energy become important, and these symmetry-induced vortex states undergo symmetry-breaking and symmetry-switching transitions that lead to a progressive recovery of the Abrikosov vortex lattice.[12,15,19–26]

These properties of individual superconducting microstructures can be also significantly modified by the inhomogeneous distribution of magnetic field produced by a ferromagnet on top of the superconductor. A good example here is the profound influence that a magnetic dot may have on the onset of superconductivity, and vortex matter in loops and disks, which may lead to asymmetric phase boundaries and to maximum critical temperatures for finite values of the applied magnetic field which are antiparallel to the magnetization of the dot.[27] Besides, a ferromagnet on top of a superconducting disk can also generate vortex-antivortex states that are competing with the symmetry-induced vortex-antivortex molecules found in mesoscopic regular polygons.[28,29] Other effects that have been observed in these heterostructures are a phase shift in superconducting loops with magnetic dots that can be applied for the design of flux-based superconducting qubits,[30] and an enhanced stability of particular vortex states along the phase boundary.[31]

Recently, we have reported that the behavior of the hybrid nanosystem formed by a mesoscopic superconducting square with a ferromagnetic dot on top is strongly different, at both $T_c(H)$ and inside the superconducting phase, from that of the individual microsquare. In particular, we have observed that along $T_c(H)$ the magnetic dot may induce an expansion of the symmetry consistent vortex-antivortex patterns and the simultaneous nucleation of several vortices (multiquanta vortex entries).[32] As a consequence of this last effect, the usual increment of the vorticity by one is broken close to the normal/superconducting transition although it is progressively restored deeper in the superconducting state. The mechanisms of this recovery of L values are not only the conventional flux expulsion already observed in individual microsuperconductors but also the spontaneous generation of additional vortices with decreasing temperature.[33] These different properties have an intrinsic interest from a fundamental point of view but, besides, they also open different paths for the control and manipulation of the flux quantization that could be used to develop new superconductor-based nanodevices.

However, for the better understanding of the physical mechanisms of these effects, as well as for the motivation of their experimental study and potential applications, it is necessary to construct a normal-superconducting phase diagram of this hybrid nanostructure analogous to those already calculated for individual mesoscopic superconductors.[15,24,25] With that purpose, in this paper we will first use the linearized Ginzburg-Landau equation (LGL) to determine the $T_c(H)$ phase boundary in a broad range of magnetic fields. This will allow us to identify the different vortex nucleation mechanisms that, depending on the compensation between the external and the stray magnetic fields, may vary from the conventional edge nucleation already observed in individual superconducting micropolygons to a center/ring nucleation and, eventually, a combination of both (complex edge nucleation). Then, by means of the full nonlinear GL functional, we will also study the stability of the nucleated vortex patterns. For that, we will calculate the normal-superconducting phase diagram of the structure down to temperatures well inside the superconducting phase. Our findings show that the stray field of the dot also affects deeply the evolution with temperature of the nucleated order parameter, giving rise to instability mechanisms that differ from those of the individual microstructure and that may lead to highly nonsymmetric vortex states. In addition, the geometry of the dot also forces the vortex matter in this hybrid S/F nanostructure to behave similarly to the case of an individual microdisk for relatively large vorticity values.

II. MODEL

Within the framework of the Ginzburg-Landau phenomenological theory, the free energy of a superconductor can be described in terms of the superconducting order parameter, Ψ, as[34]

$$G = G_n + \int \left[\Psi^\star \hat{L} \Psi + \alpha |\Psi|^2 + \frac{\beta}{2}|\Psi|^4 + \frac{(\vec{h}-\vec{H})^2}{8\pi} \right], \quad (1)$$

where $\hat{L}=\hbar^2(-i\vec{\nabla}-\frac{2\pi}{\phi_0}\vec{A})^2/2m^\star$ is the linearized GL operator, ϕ_0 is the magnetic-flux quantum, $m^\star$ is the effective mass of the Cooper pairs, α and β are the GL parameters, $\vec{h}$ and $\vec{H}$ are, respectively, the local and applied magnetic fields, G_n is the free energy of the normal state, and $\vec{A}$ is the vector potential. In presence of a disk-shaped dot magnetized parallel to the z direction and of a homogeneous external field applied perpendicularly to the sample, the latter is cylindrically symmetric and can be written as[35]

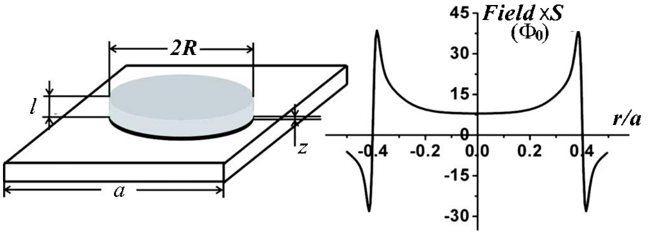

FIG. 1. (Color online) Schematic illustration of the superconducting square with the magnetic dot on top together with the field profile corresponding to a dot with $M_{\mathrm{dot}}=18\phi_0$, $R=0.4a$, thickness $l=0.033a$, and the gap $z=-0.0025a$.

$$A_\varphi^{\mathrm{total}}(r) = \frac{Hr}{2} + 4M_{\mathrm{dot}}\sqrt{\frac{R}{r}}\int_0^l dz_d \frac{\left[\left(1-\frac{k^2}{2}\right)K(k)-E(k)\right]}{k}, \quad (2)$$

with $A_r=A_z=0$. In the above equation K and E are, respectively, elliptic integrals of the first and second kinds while R, l, and M_{dot} hold for, respectively, the radius, the height, and the magnetization of the dot. Also in Eq. (2), $k^2=4Rr/[(R+r)^2+(z-z_d)^2]$ is a z-dependent dimensionless variable that, implicitly, may be used to take into account the presence of a substrate between the superconductor and the dot to avoid proximity effects. In the calculations presented in this work we have used $M_{\mathrm{dot}}=18\phi_0$, $R=0.4a$, $l=0.033a$, and $z=-0.0025a$ (here a is the length of the square), values that are comparable with the parameters of the dots used in previous experimental studies.[27] The corresponding field profile is presented in Fig. 1, together with a schematic drawing of the superconducting square with the magnetic dot on top.

In what follows we will restrict our study to a mesoscopic square with a much smaller than the magnetic penetration depth, $\lambda(T)$, and thickness d much smaller than both $\xi(T)\equiv\xi(0)/(1-T/T_{c0})$ [here $\xi(0)$ is the GL coherence length amplitude and T_{c0} is the critical temperature at zero field] and $\lambda(T)$. In this case, it is possible to neglect in Eq. (1) the variation in the order parameter across d (Ref. 12), and the modification of the magnetic field induced by screening and vortex currents.[15,24,25] Then, the GL functional can be solved in two dimensions and Eq. (1) is reduced to

$$G = G_n + \int \left[\Psi^\star \hat{L} \Psi + \alpha |\Psi|^2 + \frac{\beta}{2}|\Psi|^4 \right]. \quad (3)$$

Despite of this simplification, the minimization of the GL functional is still a complex problem since the solutions of Eq. (3) are to be found while taking into account the superconducting/vacuum boundary condition given by[34]

$$\left(\frac{\vec{\nabla}}{i} - \frac{2\pi}{\phi_0}\vec{A}\right)\Psi|_n = 0, \tag{4}$$

where n holds for the normal to the sample boundary line. However, close to the normal-superconducting phase boundary, the amplitude of the superconducting order parameter may be considered small and the fourth power on $|\Psi|$ can be neglected in Eq. (3). Subsequently, to study the nucleation of superconductivity, it suffices to solve the LGL equation, $\hat{L}\Psi = \varepsilon\Psi$. With that purpose a procedure has been developed based on a gauge transformation of the vector potential that, for both individual microsuperconductors[15,16] and hybrid S/F nanostructures with cylindrical symmetry of the ferromagnet,[15,32,33,36] leads to $A_n = 0$ along the sample boundary line[15,16] (see the Appendix for a brief description). Then, Eq. (1) is transformed into the conventional Neumann boundary condition, $\nabla\Psi|_n = 0$, and the LGL equation may be solved by using an analytic basis set. In a square, as a consequence of its fourfold symmetry, the eigenvalues of the LGL equation, ϕ_i, can be divided into four different irreducible representations (irreps) that we denote as A, B, $E+$, and $E-$. They correspond to solutions with, respectively, no vortex ($L=0$), a giant vortex ($L=+2$), a vortex ($L=+1$), and an antivortex ($L=-1$) in the center of the sample that will be surrounded by a number of vortices (multiple of four) that depends on the applied magnetic field.[15,16]

Deep in the superconducting phase, however, $|\Psi|$ cannot be any longer considered as small and the nonlinear term in Eq. (3) has to be taken into account. Nevertheless the solutions of the LGL equation can still be used to describe the symmetry effects via an expansion of the superconducting order parameter, $\Psi = \Sigma_1^N c_i \phi_i$ (here c_i are the complex coefficients of the expansion, and N is the dimension of the basis set) since these functions implicitly include the geometry constraints imposed by the boundary condition. After this Ψ expansion Eq. (3) is transformed into

$$G - G_n = \sum_i (\alpha + \epsilon_i) c_i^{\star} c_i + \frac{\beta}{2S} \sum_{ijkl} A_{ij}^{kl} c_i^{\star} c_j^{\star} c_k c_l, \tag{5}$$

where ε_i is the eigenvalue corresponding to the eigenfunction of the LGL equation ϕ_i, S is the superconductor's surface area, and $A_{ij}^{kl} = \int \phi_i^* \phi_j^* \phi_k \phi_l$ are parameters that depend on the geometry of the sample but not on its size.

Thus, to solve the nonlinear Ginzburg-Landau functional, it is only necessary to find the set of complex numbers c_i that minimize Eq. (5). For that, we have used simulated annealing method incorporating a Mersenne twister algorithm[37] as random number generator. Indeed, it is only possible to deal with a finite number of functions in the order-parameter expansion. Therefore, we have chosen a basis set formed by 24 functions (six per irrep) after checking that larger basis sets do not lead to a different result in the considered range of magnetic fields and temperatures. Prior minimization, we renormalize the coefficients c_i through $c_i \rightarrow a\sqrt{-\alpha_1/\beta}c_i'$ and, besides, we scale the energy in units of $S\alpha_1/\beta$ (here α_1 is the lowest eigenvalue of the LGL equation). As a result of these transformations, the right-hand term of Eq. (5) becomes β independent [and, thus, $\lambda(T)$ independent], which means that the obtained order parameter is independent on the κ value. Therefore, by using Eq. (5) it is possible to analyze the evolution of the vortex states in thin structures of both type-I and type-II superconductors. Furthermore, after the renormalization of both the c_i coefficients and the energy, the right-hand side of Eq. (5) only depends (besides A_{ij}^{kl}) on the ratios $(S/\xi^2 + \epsilon_i)/(S/\xi^2 + \epsilon_1)$. Therefore, the GL energy and, thus, the emerging phase diagram will be dependent only on $S/\xi^2(T)$ and ϕ/ϕ_0 (here $\phi = HS$ is the applied magnetic flux) so that they can be applied to any sample with a given S and $\xi(T)$.

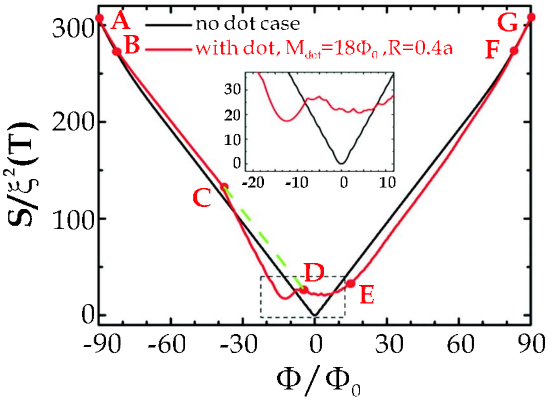

FIG. 2. (Color online) $T_c(H)$ phase boundary of the studied hybrid S/F nanostructure (red). Compared with the results for the no-dot case (black), it presents a clear asymmetric behavior with respect to the external field that is consequence of the compensation between the latter and the stray field of the dot. In particular, as shown in the inset, this compensation leads to a minimum T_c of the structure at a nonzero (and negative) field value. The letters divide the curve in six different parts accordingly with the symmetry of the nucleated order parameter. The green-dashed line is an extrapolation of the $T_c(H)$ behavior at high negative fields (where the stray field of the dot may be considered as a small perturbation) that illustrates that the compensation between both fields is maximum in the CD part.

III. LINEAR RESULTS

A. Phase boundary

The $T_c(H)$-phase boundary of the hybrid S/F structure object of our study is presented in Fig. 2, together with the results for the no-dot case. Both curves are obtained from the LGL equation as the minimum (at each ϕ value) of the lowest Landau levels (LLL) of the four different irreps, which describe the nucleation of superconductivity via $\epsilon_1 = -\alpha \equiv \hbar^2/2m^*\xi^2(T)$. Thus, the field dependence of T_c is taken into account in the figure through $\xi(T) = \xi(0)/[1 - T_c(\phi)/T_{c0}]$. As it may be seen, the phase boundary in absence of the magnetic dot is perfectly symmetric and it only depends on the applied magnetic field. Instead, analogously to the case of a magnetic dipole on top of a cylindrical superconducting sample,[38] the $T_c(H)$ curve of the hybrid structure depends on the competition between the applied magnetic field and the stray field of the dot. As a consequence, a clear asymmetric behavior with respect to the polarity of the applied field is seen. In particular, as shown in the inset, the phase boundary shifts along both the T and the ϕ axis, leading to a minimum T_c of the structure at a nonzero (and negative) field value that increases (in absolute value) with the magnetization of the dot. This fact strongly suggests the existence of a compensation effect between the external field and the stray field of the dot that has been already observed in loops and disks.[27] Furthermore, as it is now well established,[15,16] the phase boundary of the no-dot case is consequence of a well defined sequence of crossings between the LLL of the different irreps, $A \rightarrow E+ \rightarrow B \rightarrow E- \rightarrow A \ldots$, each of them leading to an increase in the vorticity by one. Instead, in a sample with a magnetic dot, some irreps are energetically favored with respect to the others so that some vorticity values are forbidden at the boundary. In the case of the magnetic disk studied in this work these vorticity values are $L=8$, 4, 2, -1, -2, -3, -6, -7, -8, -9, -11, and -13.[32] However, as we will discuss in Sec. IV, these vorticity values can be recovered by lowering the temperature well below the transition.[33]

In Fig. 2 we also divide the $T_c(H)$ curve for the magnetic dot case in six different parts (namely, AB, BC, CD, DE, EF, and FG), accordingly with the symmetry of the nucleated order parameter that we will discuss with more detail in the next subsection. For AB and FG parts the applied magnetic field is much higher than the stray field of the dot, and the effect of the latter can be neglected. Thus, the curve in these parts overlaps with the one corresponding to the no-dot case, and the order parameter nucleates likewise in an individual microsquare (i.e., with fourfold symmetry and by increasing the vorticity one by one). In what follows we will denote these parts of the phase boundary as *conventional* nucleation regimes. In contrast, along the CD part, the stray field of the dot is compensated by the external field. This is first illustrated by the fact that in this region the phase boundary falls well below the green-dashed line that extrapolates the behavior of the $T_c(H)$ boundary in the conventional nucleation regime observed at higher magnetic fields. In fact, the maximum critical temperature of the structure is also achieved in this region (at approximately $\phi=-13\phi_0$). Besides, as we discuss below, the compensation between the stray and the applied magnetic fields leads to the appearance of a superconducting disk/ring in the region of the microsquare that falls just below the dot. This order-parameter distribution favors the simultaneous entry in the sample of several vortices at some magnetic-field values. We have observed that these *multiquanta transitions* may lead to changes in the vorticity by +4, +5, and +8, and that they are associated with the long-period oscillations that the phase boundary presents in this region. Due to these particular features, we will denote this part of the $T_c(H)$ curve as *center- or ring*-nucleation regime. Finally, BC, DE, and FE parts are intermediate regimes where the nucleated order parameter presents a mixed symmetry in between the squared and cylindrical geometries of, respectively, the sample and the dot. Therefore, in what follows we will call them *complex* nucleation regimes. We have found that multiquanta transitions are still possible in these regions. In particular, we have observed jumps in L in BC (by +2 and +4) and DE (by +2) but not in EF.

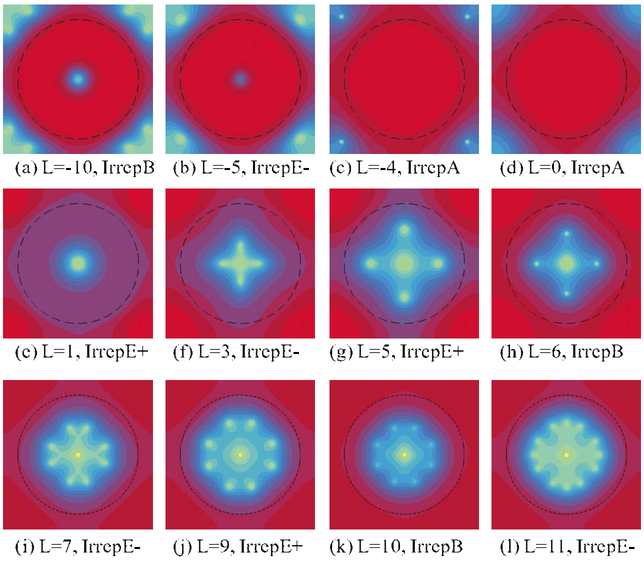
(a) L=-10, IrrepB (b) L=-5, IrrepE- (c) L=-4, IrrepA (d) L=0, IrrepA
(e) L=1, IrrepE+ (f) L=3, IrrepE- (g) L=5, IrrepE+ (h) L=6, IrrepB
(i) L=7, IrrepE- (j) L=9, IrrepE+ (k) L=10, IrrepB (l) L=11, IrrepE-

FIG. 3. (Color online) Evolution of the nucleated order parameter along the $T_c(H)$ phase boundary in the region $-24.75\phi_0 \leq \phi \leq -6.5\phi_0$. The higher values of the Cooper pair density are shown in red and the dashed circumference represents the region below the dot. Due to the compensation between the stray field of the dot and the applied magnetic field, in panels (a)–(d) the sample presents a well developed superconducting disk area at the center surrounded by four topologically equivalent corners with lower amplitude of the superconducting order parameter. These two parts of the sample present different mechanisms for the vortex nucleation: one by one inside the superconducting disk (as in an individual superconducting microstructure) and $4n$ by $4n$ in the corners (n in each corner). These mechanisms occur independently (leading to changes in the vorticity by 1 or by $4n$) or simultaneously (with a jump in the vorticity by $4n+1$). When the compensation ceases, the usual increment of the vorticity by 1 is progressively recovered although the nucleated order parameter shows a mixed symmetry between the disk and square geometries [panels (e)–(l)].

B. Vortex patterns

To illustrate the origin of the different properties of the normal-superconducting phase boundary of a microsquare with a magnetic disk on top described in the previous subsection, in Fig. 3 we present the evolution with the applied magnetic field of the squared amplitude of the superconducting order parameter ($|\Psi|^2$) along $T_c(H)$ together with the corresponding vorticity value and irrep that determines the solution. For simplicity, we have restricted ourselves to magnetic fields in the range $-24.75\phi_0 \leq \phi \leq 6.5\phi_0$, where most of the different effects associated with the nucleation of superconductivity can be observed. The higher values of the Cooper pair density are presented in red and the dashed circumference represents the region below the dot. Indeed, if we define the vortices/antivortices as flux lines parallel/antiparallel to the magnetization of the ferromagnet, one may expect that they prefer to stay inside/outside the circumference. However, this general rule has to be combined with the peculiarities of the topology of the order-parameter distribution. In particular, in the *center- or ring*-nucleation regime [panels (a)–(d)] the sample presents a highly inhomogeneous distribution of the Cooper pair density as a consequence of the compensation between the stray and applied magnetic fields. This results in the appearance of a well developed superconducting disk area in the center of the sample surrounded by four corners with a lower amplitude of the order parameter. Due to their different symmetry, these two parts of the sample also present a different mechanism for the vortex nucleation: while in the superconducting disk the vortices nucleate one by one as in an individual superconducting microstructure,[8,9] in the four topologically equivalent corners $4n$, vortices have to be simultaneously nucleated (n in each corner). Besides, the generation of vortices in these two regions of the sample may also happen *independently*. This explains why in the *center- or ring*-nucleation regime the vorticity can change by $4n$ [as in panels (d) to (c), with the simultaneous nucleation of one antivortex in each corner of the sample], by one [as in panels (c) to (b), with the nucleation of an antivortex in the center of the superconducting disk], or by five [as in panels (b) to (a), where the nucleation of vortices in the two regions of the sample occurs simultaneously].

As it may be also seen in Fig. 3 [panels (e)–(l)] for applied magnetic fields above, approximately, $-7.75\phi_0$ the vorticity of the sample changes to positive values and it enters the *complex* nucleation regime. In contrast to the *center- or ring*-nucleation regime but analogously to the case of the conventional edge-nucleation characteristic of individual micropolygons, in this magnetic-field region the corners of the square have a high Cooper pair density. However, the nucleated order parameter still has a mixed symmetry between the squared and cylindrical geometries. Panels (e)–(l) illustrate that this competition between symmetries makes particularly stable vortex patterns with a two-shell configuration, with $4n$ vortices in an outer shell and a single vortex, antivortex, or giant vortex (with, respectively, vorticity 1, −1, or 2) at the center of the square. This multishell structure, similar to the one observed in the superconducting phase of mesoscopic disks,[39,40] induces multiquanta vortex entries along the phase boundary since, for instance, the vortex states with $L=4$ and $L=8$ cannot be arranged in this configuration. Subsequently, these vorticities are absent at $T_c(H)$. The value $L=2$ is also forbidden at the boundary, probably due to the fact that the presence of an isolated giant vortex is not favored by the large peaks that the profile of the stray field has at the edges of the magnetic disk. These peaks will tend to break up the giant vortex into two single vortices that cannot be symmetrically arranged in a two-shell structure.

IV. NONLINEAR RESULTS

A. Phase diagram

In physical systems, linearity and symmetry are often directly related. Thus, the symmetry-induced properties observed close to the $T_c(H)$ boundary of mesoscopic superconductors are expected to disappear deep in the superconducting phase, where the nonlinear term in the GL-free-energy expansion becomes important. For instance, in the case of the hybrid S/F structure studied here, we have recently found that the values of the vorticity forbidden at the onset of superconductivity can be recovered with lowering of the temperature. However, how do the vortex patterns evolve with decreasing temperature? To answer this question, we first present in Fig. 4(1) the normal-superconducting phase diagram, obtained by minimizing Eq. (5), for the structure schematically shown in Fig. 1. The field interval (x axis) has been chosen to cover the range of the phase boundary where the order-parameter distributions shown in Fig. 3 nucleate. Therefore, we have identified the region of the $T_c(H)$ curve (thick solid line) corresponding to each of these nucleated vortex states by the same lower case letter than in that figure. The evolution of these vortex patterns in the superconducting phase has been studied down to temperatures as low as $S/\xi^2(T)=220$ (y axis). As in individual nanosuperconductors,[10–18] we have observed that with decreasing temperature the nucleated order parameter undergoes symmetry-switching and symmetry-breaking transitions that are represented in the figure by thin solid lines. As it can be seen, some of them (tagged with one) have a negative (positive) slope for $L>0$ ($L<0$), an indication that they are related with transitions that involve the spontaneous nucleation of vortices (antivortices) with decreasing temperature. The different vortex states have been identified in the phase diagram as follows: the capital letters from A to V correspond to the configurations found at the lowest studied temperature. So deep in the superconducting phase we observe that the usual increment of the vorticity by one is restored and, thus, these letters hold for changes in L by one from −10 to 10. For the vortex patterns obtained at higher temperatures we use the same letters for the same vorticity values followed by a number for each different spatial distribution of the order parameter (starting from zero for the closest one to the boundary). So, as it can be seen in the figure, there exist several vortex states with the same vorticity but with a different configuration, such as A and $A0$ ($L=-10$), $M1$ and M ($L=2$), $N0$ and N ($L=3$), $P0$ and P ($L=5$), $Q0$ and Q ($L=6$), $R0$, $R1$, and R ($L=7$), S and $S1$ ($L=8$), and U, $U0$, $U1$, and $U2$ ($L=10$), which result from one or several symmetry-breaking transitions. In contrast, the phases F, G, K, L, and T seem to be more stable, as they do not change their configuration during the whole temperature lowering process and they occupy a larger region of the diagram than the others. This stability can be attributed to their vorticity values ($L=-5$, −4, 0, 1, and 9, respectively), which are easy to arrange following the mixed symmetry of the sample resulting from the interplay of the square and the cylindrical geometries of, respectively, the square and the dot (see next subsection).

Figure 4(1) also illustrates that with decreasing temperature some new phases, such as B ($L=-9$), C ($L=-8$), D ($L=-7$), E ($L=-6$), H ($L=-3$), I ($L=-2$), J ($L=-1$), $M1$ and M ($L=2$), O ($L=4$), and $S1$ and S ($L=8$), are introduced into the system. Their corresponding vorticities are not revealed at the boundary so that the generation of these vortex states leads to the recovery of the usual increment of L by one. However, we have also found that some of these patterns are unstable and, thus, they can only be observed in a narrow region of the phase diagram. These configurations have been grouped in the figure in two *transition regions* (CDE and HIJ) characterized by the small energy differences between

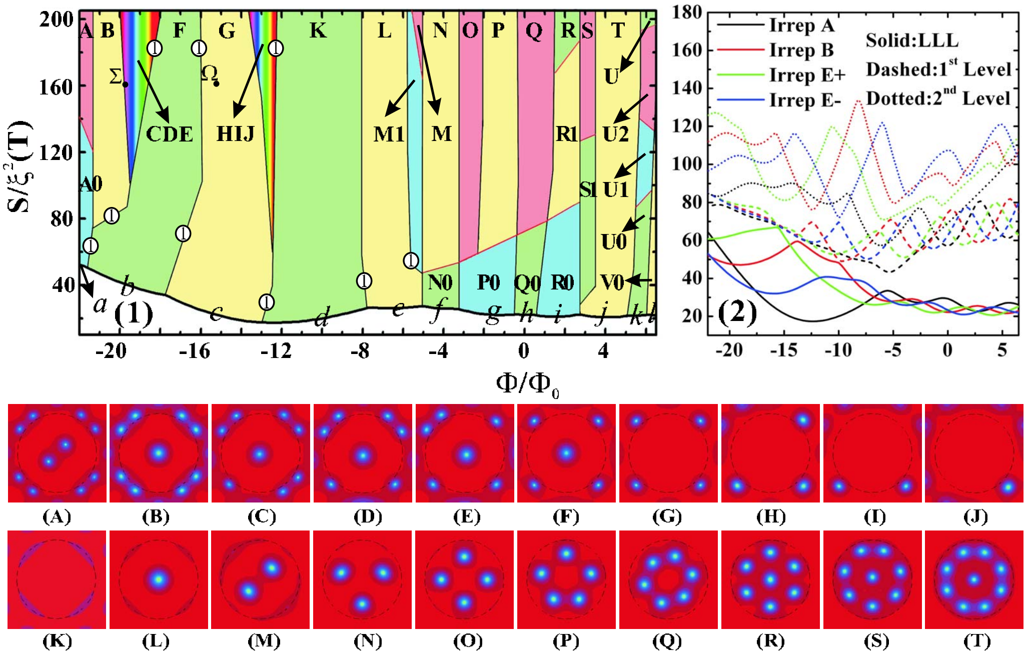

FIG. 4. (Color online) Panel (1) is the normal-superconducting phase diagram of the mesoscopic square with a magnetic dot on top shown in Fig. 1. The field interval has been chosen to cover the regime where the vortex patterns presented in Fig. 3 nucleate so that in the $T_c(H)$ curve (thick solid line) we have identified the nucleation region of each of these vortex states by using the same lower case letter than in the corresponding panel of that figure. The thin solid lines are associated with the different symmetry-breaking and symmetry-switching transitions that the order parameter undergoes in the superconducting phase. Therefore, they separate different vortex patterns that have been labeled by using upper case letters followed or not by a number, the latter corresponding to those found at the lowest studied temperature. The configurations with the same letter have the same vorticity, such as A and $A0$ ($L=-10$), $M1$ and M ($L=2$), $N0$ and N ($L=3$), $P0$ and P ($L=5$), $Q0$ and Q ($L=6$), $R0$, $R1$, and R ($L=7$), S and $S1$ ($L=8$), and U, $U0$, $U1$, and $U2$ ($L=10$). Note that the lines tagged with 1 have a negative (positive) slope for $L>0$ ($L<0$) and, thus, they correspond to transitions involving the spontaneous nucleation of vortices (antivortices) with decreasing temperature. This phenomenon may also happen in the *transition regions CDE* and *HIJ*, characterized by a high instability associated to small energy differences between the different vortex states. A first indication of the origin of this instability is shown in panel (2), where we present the ϕ dependence of the energy of the first three Landau levels of each irrep involved in the order-parameter expansion. As it can be seen, these levels are closer in energy to each other in the field regime where both *transition regions* appear than in other ϕ intervals. Panels (a)–(t) are the vortex patterns found at $S/\xi^2(T)=200$ in the magnetic-field region covered by the phase diagram presented in panel (1) [the vortex pattern corresponding to the phase U at $S/\xi^2(T)=200$ is separately shown in Fig. 5(d)]. Note that the usual increment of the vorticity by one is recovered at such a low temperature so that the vortex patterns in (a)–(t) cover L values between −10 and 9 in steps of 1. For negative vorticities, the antivortices nucleate in a well defined sequence: they first progressively fill the corners of the square in the region out of the dot and, once the corners have the same number of antivortices, the next one nucleates in the center of the square and the cycle restarts. In contrast, for positive vorticities [panels (l)–(t)] all the vortices are located in the region below the dot and they behave similarly to the case of an individual superconducting microdisk, i.e., they arrange themselves in a multishell structure trying to form a triangular lattice.

vortex states that, subsequently, will be very sensitive to small perturbations. Due to that, in these regions we have not established well defined transition lines between vortex patterns. As we will see in the next subsection, the origin of this instability arises from the difficulty in constructing vortex states with the corresponding vorticity values that comply with the symmetry of the system.

B. Vortex patterns at low temperatures

As mentioned in the previous subsection, the usual increment of the vorticity by one, absent at the $T_c(H)$ boundary due to the multiquanta vortex entries, is recovered deep inside the superconducting phase. To better illustrate this point, in Figs. 4(a), 4(c), and 4(c)–4(t) we present the vortex patters found at $S/\xi^2(T)=200$ in the magnetic-field region covered by the phase diagram of Fig. 4(1) [the vortex pattern corresponding to the phase U ($L=10$) at $S/\xi^2(T)=200$ is separately shown in Fig. 5(d)]. The letters in the panels correspond to the same phases defined in Fig. 4(1) so that they cover vorticity values from −10 to 9 in steps of 1. For completeness, we also present in Fig. 4(2) the magnetic-field dependence of the energy [in $S/\xi^2(T)$ units] of the first three Landau levels of each irrep involved in the expansion of the order parameter. Apart from the recovery of the increment of the vorticity by one, these vortex patterns also differ from those observed at $T_c(H)$ by the absence of giant vortex and vortex-antivortex states, a confirmation that these configurations are symmetry induced. However, the figure also illustrates that, as for the patterns at the boundary, the antivortices are placed or at the center of the sample, or in the region outside the dot [panels (A)–(J)] while the vortices always

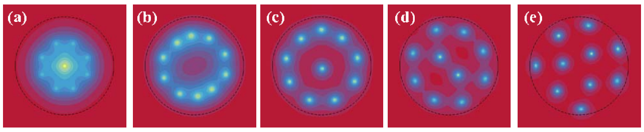

FIG. 5. (Color online) Evolution with decreasing temperature of the vortex states at $\phi=6\phi_0$ ($L=10$). (a)–(e) are the vortex patterns at $S/\xi^2(T)=40$, 120, 160, 200, and 550, respectively, and the transitions between these configurations happen at $S/\xi^2(T)=105$, 135, 195, and 470. (a) Close to the phase boundary the vortex pattern is perfectly symmetric, with a giant $2\phi_0$ vortex at the center and eight vortices in an outer shell arranged parallel to the edges of the square. (b) With decreasing temperature the giant $2\phi_0$ vortex splits, and all ten vortices, attracted by the peaks of the stray field of the dot, form a single shell structure at the border of the ferromagnet. Deeper in the superconducting phase the vortices progressively migrate to the center of the sample giving rise to the two-shell configurations in (c)–(e). As it can be seen, this process leads to a progressive recovery of a (distorted) conventional triangular lattice.

TABLE I. Moduli of the complex coefficients in the order-parameter expansion at points Σ $[S/\xi^2(T)=160$ and $\phi=-19.90\phi_0]$ and Ω $[S/\xi^2(T)=160$ and $\phi=-15\phi_0]$ in Fig. 4(1).

	Point Ω			
	Irrep *A*	Irrep *B*	Irrep *E*+	Irrep *E*−
LLL	1791.25	0.01	0.24	0.17
First level	857.27	0.04	0.19	0.23
Second level	23.04	0.02	0.04	0.02
Third level	211.17	0.01	0.05	0.07
Fourth level	103.79	0.01	0.03	0.02
Fifth level	0.77	0.01	0.01	0.02
	Point Σ			
LLL	107.39	107.94	124.47	1526.78
First level	451.09	247.88	333.18	411.40
Second level	182.25	26.79	48.77	59.74
Third level	66.77	74.01	27.91	42.93
Fourth level	32.68	13.84	79.05	159.83
Fifth level	93.14	13.10	17.84	89.39

arrange themselves just below the ferromagnet [panels (L)–(T)].

From Fig. 4 it is also possible to infer that the mechanism for the nucleation of antivortices obeys the following rule: starting at zero vorticity [panel (K)], the antivortices first progressively fill the corners of the square [panels (J) with $L=-1$, (I) with $L=-2$, (H) with $L=-3$, and (G) with $L=-4$]. Once each of the corners has an antivortex, the next one nucleates at the center of the sample [panel (F) with $L=-5$], and then, the sequence starts again. This mechanism, which gives rise to nonsymmetric vortex states, governs the nucleation of antivortices up to $L=-15$. In contrast, as shown in panels (L)–(T), for positive L values the symmetry of the order-parameter distribution is controlled by the cylindrical geometry of the dot. As a consequence, the vortex patterns behave similarly to those of an individual superconducting disk, i.e., deep inside the superconducting phase the symmetric states at the boundary split into individual vortices that arrange themselves into a multishell structure trying to form a conventional triangular lattice.[39,40] The crossover between both regimes of nucleation of vortices and antivortices appears at, approximately, $\phi=-8.5\phi_0$ [see Fig. 4(1)], in agreement with the magnetic field that would compensate the average field of the dot in the superconductor. The latter can be obtained by integrating the field profile shown in Fig. 1 over the microsquare, which gives a result of $\phi\simeq10\phi_0$.

In the previous subsection we have already pointed out the existence in the phase diagram of two transition regions (*CDE* and *HIJ*) where the vortex patterns are highly unstable. The origin of this instability may be understood by first taking into account that, as discussed in Sec. II, in our calculations the solution of the nonlinear GL functional is constructed by linear combination of the first six Landau levels of each irrep. Figure 4(2), where we present the field dependence of the first three, illustrates that these energy levels are closer to each other for magnetic fields in the field regime where both transition regions appear (approximately $-20.25\phi_0\leq\phi\leq-12.50\phi_0$) than in other ϕ regions (note, in particular, the small energy differences between the first Landau levels of each irrep, and between these levels and the lowest Landau levels of irreps $E+$ and B). These small differences in energy between the functions involved in the expansion of the order parameter are a first indication of a possible instability in this region. However, what actually determines the final vortex pattern and its stability is the set of temperature and field dependent complex coefficients of the ϕ expansion that minimize the full GL functional at each point of the phase diagram. To illustrate this, in Table I we present the moduli of the complex coefficients obtained at points Σ $[S/\xi^2(T)=160$ and $\phi=-19.90\phi_0]$ and Ω $[S/\xi^2(T)=160$ and $\phi=-15\phi_0]$ of Fig. 4(1). As it can be seen, at point Σ only the levels corresponding to irrep A give a significant contribution to the final solution. This means that there is no admixture between different irreps and, thus, between different symmetries,[24,25] which leads to the symmetric pattern with four antivortices in the corners shown in Fig. 4(g). Besides, although Fig. 4(2) shows that the levels are close in energy in this field region, the data in the table also indicate that there exist large differences between the coefficients of the functions significantly involved in the Ψ expansion, which results in a strengthening of the stability of the obtained state. This admixture of energy levels of a single irrep also occurs at all the points of phases G [Fig. 4(g), $L=-4$, irrep A], F [Fig. 4(f), $L=-5$, irrep $E-$], K [Fig. 4(k), $L=0$, irrep A], L [Fig. 4(l), $L=1$, irrep $E+$], and T [Fig. 4(t), $L=9$, irrep $E+$], and it also leads to symmetric vortex patterns at low temperatures in these regions. In fact, these vortex states show almost no change with respect to the nucleated ones with the same vorticity [see Fig. 3], indicating the strong stability of these configurations with varying temperature.

The situation is different at point Σ, where the LLL of irrep $E-$ admixes with excited levels of the other irreps. As we know from the previous works in individual microsuperconductors,[24,25] this combination between irreps gives rise to nonsymmetric vortex states, as the one with L

$=-8$ that corresponds to this point [Fig. 4(c)]. However, in individual structures asymmetry arises from the combination of no more than three energy levels.[24,25] In contrast, the data in Table I show that the LLL of irrep $E-$ has a significant admixture with at least the first-excited levels of all irreps with similar coefficients. Moreover, as shown in Fig. 4(2), these energy levels also have a similar energy. As a consequence, this vortex pattern will be very sensitive to small perturbations such as tiny variations in the temperature and the applied magnetic field. In fact, we have found that around this point the order-parameter distribution immediately jumps from Fig. 4(c) to Fig. 4(b) and 4(d), or 4(e) with small changes in ϕ and T. A similar behavior can be observed at all the points of the transition regions *CDE* and *HIJ*. Consequently, we have not separated the vortex states in these parts of the phase diagram.

C. Evolution of the vortex states

It is known from previous studies on individual mesoscopic superconductors that in the superconducting phase the nucleated order parameter may undergo four different types of symmetry-breaking or symmetry-switching transitions: second-order transitions with conservation of both symmetry and vorticity, first-order symmetry-breaking transitions with vorticity change, first-order symmetry-switching transitions with vorticity change, and second-order symmetry-breaking transitions with vorticity conservation.[24,25] Apart from the first one, which has only been observed in triangles due to the coincidence of the geometry of the sample and the symmetry of the Abrikosov lattice,[25] these different types of transitions are also present in the phase diagram of the hybrid S/F structure studied here. For instance, the second one may be found at low temperatures by changing the field. Then it is possible to observe transitions between a symmetric state and a nonsymmetric one with different vorticity, as the one between phases *G* and *H* (see Fig. 4). The third type can be observed if, for instance, we decrease the temperature from $T_c(H)$ down to $S/\xi^2(T)=100$ at a magnetic field of $\phi=-18\phi_0$ [see Fig. 4]. Then the order parameter changes from the nucleated one, given by Fig. 3(c), to the configuration shown in Fig. 4(f), which corresponds to a transition between two symmetric states with different vorticity. The last type includes the splitting of the giant vortex state and the vortex-antivortex annihilation.[24,25] In Fig. 4(1) these processes correspond to the transitions between phases *A*0 [Fig. 3(a)] and *A* [Fig. 4(a)] (giant vortex splitting for $L=-10$), *Q*0 [Fig. 3(h)] and *Q* [Fig. 4(q)] (giant vortex splitting for $L=6$), and *N*0 [Fig. 3(f)] and *N* [Fig. 4(n)] (vortex-antivortex annihilation for $L=3$).

Figure 4(1) also shows that in this hybrid S/F nanostructure the evolution of the order parameter from the configuration nucleated at $T_c(H)$ to the vortex pattern observed at the lowest studied temperature may involve several phase transitions, in particular for positive and relatively large vorticity values ($L\geq 7$) due to the appearance of the characteristic multishell structure of a superconducting microdisk. For instance, the vortex-antivortex annihilation for $L=7$ has an intermediate phase (*R*1) between the nucleated order parameter *R*0 [Fig. 3(i)] and the final configuration *R* [Fig. 4(r)]. Even more complex is the sequence of transitions that the nucleated giant vortex state corresponding to $L=10$ [phase *U*0, Fig. 3(k)] undergoes with decreasing temperature. This sequence is shown in Fig. 5, where we present the vortex patterns that can be found at $\phi=6\phi_0$ from the vicinity of the phase boundary down to temperatures as low as $S/\xi^2(T)=550$. Figure 5(a) has been obtained at $S/\xi^2(T)=40$ and corresponds to phase *U*0. As this temperature is very close to $T_c(H)$ [$S/\xi^2(T)\simeq 22$], the geometry of the sample still dominates the spatial distribution of the order parameter, giving rise to a well defined symmetric vortex pattern with a giant vortex at the center surrounded by eight vortices parallel to the edges of the square.

However, with decreasing temperature the confinement effects become weaker, which results first in a second-order phase transition associated with the splitting of the giant vortex. The ten individual vortices are then attracted to the edges of the magnetic dot by the large positive peaks of its stray field, forming the vortex pattern shown in Fig. 5(b) [phase *U*1 at $S/\xi^2(T)=105$]. Deeper in the superconducting phase, we have found that the order parameter undergoes up to three second-order phase transitions more, which correspond to a gradual migration of vortices with lowering temperature from the outer shell below the border of the dot to the center of the sample. This process progressively generates vortex patterns with one [Fig. 5(c), calculated at $S/\xi^2(T)=120$ and that corresponds to phase *U*2], two [Fig. 5(d), calculated at $S/\xi^2(T)=200$ and that corresponds to phase *U*], and three [Fig. 5(e), if we penetrate the superconducting phase down to temperatures as low as $S/\xi^2(T)=550$] vortices in an inner shell surrounded by the remaining vortices in an outer shell. Each transition leads to a vortex pattern more triangular than the previous one, thus confirming the expected tendency to recover at low temperatures the triangular Abrikosov lattice characteristic of bulk superconductors.

Besides, these results also illustrate that, at low temperatures and relatively large *L* values, the geometry of the dot induces in this hybrid nanostructure a behavior of the vortex matter similar to that of an individual superconducting microdisk, where the configurations shown in Figs. 5(c)–5(e) have been experimentally observed in Ref. 40. In that work, however, these vortex patterns were found by repeating the experiment several times at the same temperature and magnetic field, being Fig. 5(d) the state found more frequently. In contrast, our calculations show that at a given temperature only one stable structure should be observed. The metastability found experimentally can be attributed to the small energy differences between these configurations, which can be easily overcome by small experimental perturbations.

Another interesting aspect and quite counterintuitive of the vortex matter in hybrid S/F nanostructures is the fact that vortices can be generated with lowering temperature.[33] This is in clear contrast with the behavior found in individual microsuperconductors, where only flux expulsion and the subsequent decrease in the vorticity can be observed under a temperature decrease.[15,24,25] In Fig. 4(1), the lines corresponding to transitions that involve this spontaneous vortex generation have been labeled with 1 and they can be distinguished by their slope, which opposes that of the lines associated with conventional (flux-expulsive) transitions (i.e., it is negative for $L>0$ and positive for $L<0$). Besides, the spontaneous generation of vortices can also be found in the two transition regions *CDE* and *HIJ* although, as already discussed, it is difficult to establish the lines that divide the different vortex states in these regimes.

In Ref. 33 we have already discussed the spontaneous generation of vortices at $\phi=-12.8\phi_0$, which falls in the region *HIJ* at low temperatures. In this case the nucleated order parameter corresponds to a $L=0$ state but when the temperature is decreased, four antivortices are simultaneously generated at the corners of the square. Deeper in the superconducting phase these antivortices are expelled from the sample one by one, giving rise to a sequence of transitions $L=0\rightarrow-4\rightarrow-3\rightarrow-2\rightarrow-1$ that leads to the recovery of the last three vorticity values, which are absent at $T_c(H)$. A similar behavior can be observed in the transition region *CDE* if we decrease the temperature from the boundary down to $S/\xi^2(T)=220$ at $\phi\simeq-19\phi_0$. The nucleated order parameter is given by Fig. 3(b) ($L=-5$) but when the temperature is lowered below $S/\xi^2(T)\simeq 90$ four antivortices are spontaneously created in the corners of the square, leading to a vortex pattern with $L=-9$ as the one shown in Fig. 4(b). Then, further decrease in temperature also leads to the recovery of vorticity values absent at the boundary by the expulsion of an antivortex at $S/\xi^2(T)=160$ [Fig. 4(c), $L=-8$] and at $S/\xi^2(T)=180$ [Fig. 4(d), $L=-7$].

This series of transitions is associated with a sequence of different admixtures between different energy levels: the nucleated order parameter [Fig. 3(b)] is determined by the LLL of irrep $E-$, and with decreasing temperature, it first admixes with the first and fourth Landau levels of the same irrep to create the vortex pattern with $L=-9$ given by Fig. 4(b). Deeper in the superconducting state this combination starts to admix with the first-excited level of irrep A, and the vortex states with $L=-8$ and -7 are progressively recovered with the graduated increase with decreasing temperature of the coefficient of this level in the order-parameter expansion. Other transitions that involve the nucleation of vortices with decreasing temperature can be observed in Fig. 4 beyond those related with the instability regions. This is the case of the shift from $L=1$ [phase L, Fig. 4(l)] to $L=2$ [phase $M1$ or M, Fig. 4(m)] at magnetic fields around $\phi=-5.25\phi_0$, which has been already discussed in Ref. 33. Another example is the transition between $L=0$ and $L=1$ that can be observed at $\phi\simeq-8.25\phi_0$, and that corresponds to a symmetry switch between the lowest Landau levels of irreps A [Fig. 3(d) or 4(k)] and $E+$ [Fig. 3(e) or 4(l)]. Similar switches between symmetric states by a spontaneous generation of vortices can be observed between phases G and F at $\phi\simeq-17\phi_0$, and between phases F and $A0$ at $\phi\simeq-21\phi_0$.

In previous works we have shown that in superconducting nanostructures the transitions that the vortex states undergo with decreasing temperature leave traces that can be measured in the differential magnetization, $\Delta M\times S/\Delta[S/\xi^2(T)]$, thus opening a possibility to investigate the superconducting phase of mesoscopic superconductors beyond the complex vortex imaging techniques.[25,33] In Fig. 6 we present three examples of the evolution with temperature at a constant magnetic field of this observable, obtained by using $M=\frac{1}{2cs}\int\vec{r}\times\vec{j}$ for the averaged magnetization (here c is the speed of light and $\vec{j}$ is the supercurrent). The black line with open squares has been obtained at $\phi=6\phi_0$ so that it corresponds to the sequence of transitions between vortex states presented in Fig. 5 for $L=10$. The inset shows a zoom of this curve in the dashed area, where it presents a jump in the differential magnetization at $S/\xi^2(T)\simeq 105$ associated with the splitting of the giant vortex and the subsequent transition between the configurations given by Figs. 5(a) and 5(b). More pronounced peaks can be observed at $S/\xi^2(T)\simeq 135$ and $S/\xi^2(T)\simeq 190$, which correspond to the migration of vortices from the outer shell to the center of the sample that leads to the transitions between, respectively, Figs. 5(b) and 5(c), and Figs. 5(c) and 5(d).

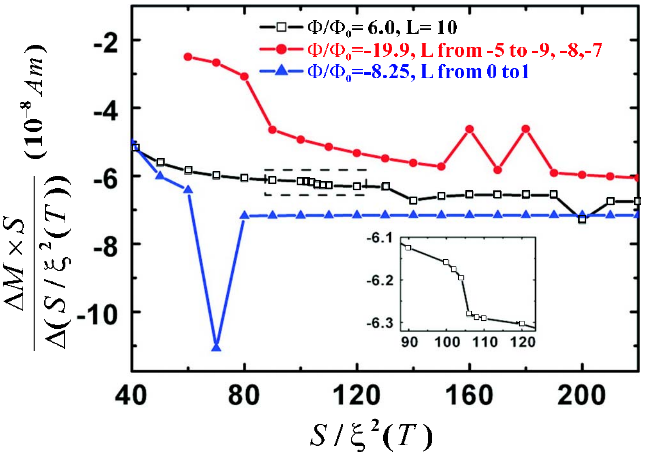

FIG. 6. (Color online) Temperature dependence of the differential magnetization at $\phi=6\phi_0$ (black line with open squares), $\phi=-19.9\phi_0$ (red line with full circles), and $\phi=-8.25\phi_0$ (blue line with full triangles). The inset is a zoom of the dashed area where a jump at $S/\xi^2(T)\simeq 105$ can be observed. This effect is associated with the transition from Fig. 5(a) to Fig. 5(b) while the other two peaks in this curve correspond to the shifts between Figs. 5(b) and 5(c) [$S/\xi^2(T)\simeq 135$] and between Figs. 5(c) and 5(d) [$S/\xi^2(T)\simeq 190$]. The peaks and jumps in the red curve are linked to the sequence of transitions $L=-5$ [Fig. 3(b)] $\rightarrow-9$ [Fig. 4(b)] $\rightarrow-8$ [Fig. 4(c)] $\rightarrow-7$ [Fig. 4(d)] that can be observed at the corresponding magnetic field. The blue curve presents a single peak linked to the spontaneous generation of a vortex in the transition between the $L=0$ [Fig. 3(d) or 4(k)] and $L=1$ [Fig. 3(e) or 4(l)] states found at $\phi=-8.25\phi_0$.

The red line with full circles has been calculated for $\phi=-19.9\phi_0$ and, as it can be seen, it shows jumps at $S/\xi^2(T)\simeq 90$, 160, and 180. As discussed in the previous paragraph, these are the temperatures at which the transitions of the sequence $L=-5$ [Fig. 3(b)] $\rightarrow-9$ [Fig. 4(b)] $\rightarrow-8$ [Fig. 4(c)] $\rightarrow-7$ [Fig. 4(d)] observed at this field occur. Finally, the blue line with full triangles corresponds to the evolution with temperature of the differential magnetization at $\phi=-8.25\phi_0$. For this magnetic field only a single peak at $S/\xi^2(T)\simeq 70$ can be observed, which is associated with the spontaneous generation of a vortex in the transition from $L=0$ to $L=1$ [i.e., from Fig. 3(d) or 4(k) to Fig. 3(e) or 4(l)] commented above. Note that, in an individual microsquare with a typical thickness of

20 nm, the $\Delta M \times S/\Delta[S/\xi^2(T)]$ amplitude in Fig. 6 will lead to magnetic moments of the order of 10^{-15} A m^2. Therefore, these jumps and peaks in the differential magnetization could be measured on arrays of 10^6 structures or so by using conventional superconducting quantum interference device (SQUID) magnetometers, which have a typical resolution of the order of 10^{-10} A m^2.

V. CONCLUSIONS

To summarize, a magnetic dot on top of a microsquare affects strongly the topology of the order-parameter distribution, giving rise to different effects for the vortex matter in hybrid S/F nanosystems. At the normal-superconducting transition, the compensation between the stray field of the dot and a homogeneous external field leads to an asymmetric $T_c(H)$ boundary with long-period oscillations. The latter are associated with the appearance in the superconductor of a well developed superconducting disk area in the region below the magnet, which is surrounded by four corners with a lower Cooper pair density. These two parts of the sample have independent mechanisms for the vortex nucleation (a simultaneous nucleation of $4n$ vortices in the corners and a vorticity increase of one by one in the center) that may give raise to multiquanta vortex entries along the $T_c(H)$ curve. This *center- or ring*-nucleation regime is in contrast with the conventional *edge*-nucleation regime found in individual microsuperconductors, which can be also observed in this hybrid nanostructure at high applied magnetic fields, where the stray field of the dot can be considered as a weak perturbation. At intermediate fields the nucleation of superconductivity in the system is a combination of both mechanisms that we have identified as a *complex edge*-nucleation regime.

As in individual superconductors, in this hybrid system the nucleated order parameter undergoes symmetry-breaking and symmetry-switching transitions when the temperature is lowered well below the phase boundary that can be experimentally studied, either by local vortex imaging techniques or by the measurable traces they leave in the differential magnetization. However, this evolution with temperature of the vortex patterns also presents significant differences with the behavior observed in individual microstructures. In particular, the vorticity values absent at the boundary due to the multiquanta vortex entries are recovered deep in the superconducting phase, a process that in some cases may involve the spontaneous generation of vortices with decreasing temperature. The field of the dot also leads to distortions of the energy levels of the system. Their admixture governs the transitions between the different configurations of the order parameter. This results in the appearance in some regions of the phase diagram of unstable and highly nonsymmetric vortex states that will be very sensitive to weak perturbations.

The geometry of the dot also controls the vortex matter of the hybrid structure at relatively large and positive L values. In this regime the flux lines are confined in the region below the magnet, where they behave similarly to the case of a superconducting microdisk, i.e., they arrange themselves in a multishell structure trying to form a distorted triangular lattice.

Other aspects of the confinement effects in hybrid S/F nanosystems, as the influence of generalized boundary conditions, proximity effects, and different geometries, and types of magnetic dots deserve further studies. Of particular interest could be the case of mesoscopic superconducting structures with attached Permalloy dots, in which magnetization is perpendicular at the center but it progressively curls around this axis when moving toward the edge of the disk.[41] This effect is tunable by the external field, and it has been already used to design a linear magnetic-flux amplifier for SQUID applications consisting of a superconducting loop enclosing a Permalloy dot.[42] Besides, it has been recently reported that an enhancement of the vortex pinning in superconducting films with Permalloy dot arrays takes place, which has been attributed to a strong local suppression of the superconductivity by the large out-of-plane component of the stray magnetic fields generated by the Permalloy disks.[43] In view of this last result, a stronger confinement of the vortices in the region below the dot (or expulsion of the antivortices to the region outside) could be expected in mesoscopic superconductors with Permalloy disks.

ACKNOWLEDGMENTS

This work has been supported by the Methusalem funding by Flemish Government, the Research Fund K.U. Leuven Contract No. GOA/2004/02, BIL China/Flanders, the Belgian Interuniversity Attraction Poles, and the Fund for Scientific Research Flanders (FWO). C.C. also acknowledges financial support from the AQDJJ and NES Programmes of the European Science Foundation, from Ministerio de Ciencia e Innovación (Spain) through Contract No. FIS2007-63709, and from Xunta de Galicia (Spain) through the Isidro Parga-Pondal Programme.

APPENDIX: GAUGE TRANSFORMATION OF VECTOR POTENTIALS WITH RADIAL SYMMETRY FOR REGULAR POLYGONS

Let us consider the case of a regular polygon with N edges under a magnetic field which, corresponding to vector potential, has radial symmetry so that $\mathbf{A}(\mathbf{r})=A(r)\hat{\varphi}$. At the edge of the polygon, this vector potential has a normal component to the boundary given by (see Refs. 15 and 36)

$$A_n = A\left(\frac{a}{2\cos\varphi}\right)\sin\varphi, \tag{A1}$$

where φ is the polar angle and $a=2r\cos\varphi$ is the diameter of the circumference inscribed in the polygon. To obtain a vector potential tangential to the edges, this normal component has to be suppressed. With that purpose, the following gauge transformation is introduced:

$$\mathbf{A}' = \mathbf{A} + \vec{\nabla} S, \tag{A2}$$

where $\mathbf{A}'$ is the new vector potential and S is an arbitrary scalar function that has to be found from the condition $A'_n=0$. Alternatively, this constrain may be written as

$$A_n = -\nabla_n S, \tag{A3}$$

which has to be fulfilled at each edge of the polygon. Besides, the rotational symmetry of the polygon has to be kept in $\mathbf{A}'$. Subsequently, S should be a periodic function on φ with period $\alpha = 2\pi/N$. As discussed in Refs. 15 and 36, the simplest possible choice for S verifying these conditions is

$$S_N(r,\varphi) = R_N(r)\sin(N\varphi), \tag{A4}$$

The substitution of Eqs. (A1) and (A4) into Eq. (A3), after eliminating the r variable by using

$$r = \frac{2}{2\cos\varphi},$$

$$\frac{\partial}{\partial r} = \frac{2\cos^2\varphi}{a\sin\varphi}\frac{\partial}{\partial\varphi}, \tag{A5}$$

leads to

$$R_N'(\varphi) + \xi(\varphi)\tilde{R}_N(\varphi) = \eta(\varphi), \tag{A6}$$

where the prime means the first derivative with respect to φ and the following notation has been introduced:

$$\tilde{R}_N(\varphi) = R_N\left(\frac{a}{2\cos\varphi}\right),$$

$$\xi(\varphi) = -N\cot(N\varphi)\tan^2\varphi,$$

$$\eta(\varphi) = A\left(\frac{a}{2\cos\varphi}\right)\frac{a\csc(N\varphi)\tan^2\varphi}{2\cos\varphi}. \tag{A7}$$

The general solution of differential Eq. (A6) is given by

$$\tilde{R}_N(\varphi) = \frac{1}{\mu(\varphi)}\left[\int \eta(\varphi)\mu(\varphi)\mathrm{d}\varphi + C_1\right],$$

$$\mu(\varphi) = \exp\left[\int \xi(\varphi)\mathrm{d}\varphi\right], \tag{A8}$$

where C_1 is a constant to be chosen so that it does not generate divergent components in both $\mathbf{A}'$ and $\nabla\cdot\mathbf{A}'$ (note that the transformed vector potential does not obey the Coulomb gauge, $\nabla\cdot\mathbf{A}'=0$). Both conditions are fulfilled with the simplest choice $C_1=0$.[15,36] Then, by using the transformation $a/2\cos\varphi \to r$ and Eqs. (A2), (A6), and (A7), the polar coordinates of the vector potential can be obtained as

$$A_r' = \frac{\partial R_N(r)}{\partial r}\sin(N\varphi),$$

$$A_\varphi' = A(r) + \frac{N}{r}R_N(r)\cos(N\varphi). \tag{A9}$$

In the case of a square under a homogeneous applied magnetic field, $\mathbf{A}=\frac{1}{2}\mathbf{H}\times\mathbf{r}$, the transformed vector potential can be analytically calculated from the above equations; the results being[15,36]

$$A_r' = -\frac{1}{4\sqrt{2}}Ha(1+z)^{3/2}$$
$$\times[-1+z+(1+2z-z^2)e^{-z}Ei(z)]\sin(4\varphi),$$

$$A_\varphi' = \frac{1}{2}Hr + \frac{1}{2\sqrt{2}}Ha(1+z)^{3/2}[1-ze^{-z}Ei(z)]\cos(4\varphi),$$

$$z = 2(r/a)^2 - 1, \tag{A10}$$

where $Ei(z)$ is the exponential integral function. However, for the square with a magnetic disk on top, the complexity of the vector potential associated to the stray field of the dot makes difficult to solve, even numerically, the integrations required to calculate R_N. To avoid this problem, we have approached the field of the dot by using rational functions. Indeed, there are infinite possible choices but we have found that a sum of three rational functions (two of them constructed as a five degree polynomial in the denominator and a six degree polynomial in the denominator, and the other one as a polynomial of degree one divided by a polynomial of degree two) gives an accuracy better than 0.01% for the approximated field of the dot.

---

*carlos.carballeira@usc.es

[1] I. F. Lyuksyutov and V. L. Pokrivsky, Adv. Phys. **54**, 57 (2004); A. I. Buzdin, Rev. Mod. Phys. **77**, 935 (2005).

[2] J. Y. Gu, C.-Y. You, J. S. Jiang, J. Pearson, Ya. B. Bazaliy, and S. D. Bader, Phys. Rev. Lett. **89**, 267001 (2002).

[3] A. I. Buzdin and A. S. Mel'nikov, Phys. Rev. B **67**, 020503(R) (2003); A. Yu. Aladyshkin, A. I. Buzdin, A. A. Fraerman, A. S. Mel'nikov, D. A. Ryzhov, and A. V. Sokolov, *ibid.* **68**, 184508 (2003); A. Yu. Aladyshkin and V. V. Moshchalkov, *ibid.* **74**, 064503 (2006).

[4] Z. Yang, M. Lange, A. Volodin, R. Szymczak, and V. V. Moshchalkov, Nature Mater. **3**, 793 (2004).

[5] W. Gillijns, A. Yu. Aladyshkin, M. Lange, M. J. Van Bael, and V. V. Moshchalkov, Phys. Rev. Lett. **95**, 227003 (2005).

[6] M. Lange, M. J. Van Bael, Y. Bruynseraede, and V. V. Moshchalkov, Phys. Rev. Lett. **90**, 197006 (2003).

[7] M. J. Van Bael, M. Lange, S. Raedts, V. V. Moshchalkov, A. N. Grigorenko, and S. J. Bending, Phys. Rev. B **68**, 014509 (2003); Q. H. Chen, G. Teniers, B. B. Jin, and V. V. Moshchalkov, *ibid.* **73**, 014506 (2006).

[8] V. V. Moshchalkov, Y. Bruynseraede, L. Van Look, M. J. Van Bael, and A. Tonomura, in *Handbook of Nanostructured Materials and Nanotechnology*, edited by H. S. Naiwa (Academic, San Diego, 1999), Vol. 3, Chap. 9, p. 451.

[9] V. V. Moshchalkov, L. Gielen, C. Strunk, R. Jonckheere, X. Qiu, C. Van Haesendonck, and Y. Bruynseraede, Nature (London) **373**, 319 (1995).

[10] D. Saint-James, Phys. Lett. **15**, 13 (1965).

[11] H. J. Fink and A. G. Presson, Phys. Rev. **151**, 219 (1966).
[12] V. A. Schweigert, F. M. Peeters, and P. S. Deo, Phys. Rev. Lett. **81**, 2783 (1998).
[13] L. F. Chibotaru, A. Ceulemans, V. Bruyndoncx, and V. V. Moshchalkov, Phys. Rev. Lett. **86**, 1323 (2001).
[14] V. R. Misko, V. M. Fomin, J. T. Devreese, and V. V. Moshchalkov, Phys. Rev. Lett. **90**, 147003 (2003).
[15] L. F. Chibotaru, A. Ceulemans, M. Morelle, G. Teniers, C. Carballeira, and V. V. Moshchalkov, J. Math. Phys. **46**, 095108 (2005).
[16] L. F. Chibotaru, A. Ceulemans, V. Bruyndoncx, and V. V. Moshchalkov, Nature (London) **408**, 833 (2000).
[17] J. Bonča and V. V. Kabanov, Phys. Rev. B **65**, 012509 (2001).
[18] A. S. Mel'nikov, I. M. Nefedov, D. A. Ryzhov, I. A. Shereshevskii, V. M. Vinokur, and P. P. Vysheslavtsev, Phys. Rev. B **65**, 140503(R) (2002).
[19] V. A. Schweigert and F. M. Peeters, Phys. Rev. Lett. **83**, 2409 (1999).
[20] J. J. Palacios, Phys. Rev. Lett. **84**, 1796 (2000).
[21] G. F. Zharkov, Phys. Rev. B **63**, 224513 (2001).
[22] B. J. Baelus and F. M. Peeters, Phys. Rev. B **65**, 104515 (2002).
[23] T. Mertelj and V. V. Kabanov, Phys. Rev. B **67**, 134527 (2003).
[24] L. F. Chibotaru, G. Teniers, A. Ceulemans, and V. V. Moshchalkov, Phys. Rev. B **70**, 094505 (2004).
[25] C. Carballeira, G. Teniers, V. V. Moshchalkov, L. F. Chibotaru, and A. Ceulemans, Europhys. Lett. **75**, 936 (2006).
[26] M. Morelle, J. Bekaert, and V. V. Moshchalkov, Phys. Rev. B **70**, 094503 (2004).
[27] D. S. Golubović, W. V. Pogosov, M. Morelle, and V. V. Moshchalkov, Appl. Phys. Lett. **83**, 1593 (2003); Phys. Rev. B **68**, 172503 (2003); Europhys. Lett. **65**, 546 (2004).
[28] M. V. Milošević, S. V. Yampolskii, and F. M. Peeters, Phys. Rev. B **66**, 024515 (2002).
[29] M. V. Milošević, G. R. Berdiyorov, and F. M. Peeters, Phys. Rev. B **75**, 052502 (2007).
[30] D. S. Golubović, W. V. Pogosov, M. Morelle, and V. V. Moshchalkov, Phys. Rev. Lett. **92**, 177904 (2004).
[31] D. S. Golubović, M. V. Milosevic, F. M. Peeters, and V. V. Moshchalkov, Phys. Rev. B **71**, 180502(R) (2005).
[32] C. Carballeira, V. V. Moshchalkov, L. F. Chibotaru, and A. Ceulemans, Phys. Rev. Lett. **95**, 237003 (2005).
[33] Q. H. Chen, C. Carballeira, and V. V. Moshchalkov, Phys. Rev. B **74**, 214519 (2006).
[34] See, e.g., M. Tinkham, *Introduction to Superconductivity* (McGraw-Hill, New York, 1996), Chap. 4.
[35] L. D. Landau and E. M. Lifshitz, *Electrodynamics of Continuum Media*, 2nd ed. (Pergamon, Oxford, 1984).
[36] L. F. Chibotaru, A. Ceulemans, G. Teniers, V. Bruyndoncx, and V. V. Moshchalkov, Eur. Phys. J. B **27**, 341 (2002).
[37] M. Matsumoto and T. Nishimura, ACM Trans. Model. Comput. Simul. **8**, 3 (1998).
[38] A. Yu. Aladyshkin, D. A. Ryzhov, A. V. Samokhvalov, D. A. Savinov, A. S. Mel'nikov, and V. V. Moshchalkov, Phys. Rev. B **75**, 184519 (2007).
[39] S. Erdin, Phys. Rev. B **72**, 014522 (2005).
[40] I. V. Grigorieva, W. Escoffier, J. Richardson, L. Y. Vinnikov, S. Dubonos, and V. Oboznov, Phys. Rev. Lett. **96**, 077005 (2006).
[41] See, e.g., R. P. Cowburn, D. K. Koltsov, A. O. Adeyeye, M. E. Welland, and D. M. Tricker, Phys. Rev. Lett. **83**, 1042 (1999); T. Shinjo, T. Okuno, R. Hassdorf, K. Shigeto, and T. Ono, Science **289**, 930 (2000); C. A. Ross, S. Haratani, F. J. Castaño, Y. Hao, M. Hwang, M. Shima, J. Y. Chen, B. Vogelli, M. Farhoud, M. Walsh, and H. I. Smith, J. Appl. Phys. **91**, 6848 (2002); A. Wachowiak, J. Wiebe, M. Bode, O. Pietzsch, M. Morgenstern, and R. Wiesendanger, Science **298**, 577 (2002).
[42] D. S. Golubovic and V. V. Moshchalkov, Appl. Phys. Lett. **87**, 142501 (2005).
[43] A. Hoffmann, L. Fumagalli, N. Jahedi, J. C. Sautner, J. E. Pearson, G. Mihajlovic, and V. Metlushko, Phys. Rev. B **77**, 060506(R) (2008).